HHS Public Access

Author manuscript

*Exp Eye Res*. Author manuscript; available in PMC 2024 July 02.

Published in final edited form as:

*Exp Eye Res*. 2024 January ; 238: 109729. doi:10.1016/j.exer.2023.109729.

# Mouse model of radiation retinopathy reveals vascular and neuronal injury

**Emily Liu**[1], **Michelle R. Tamplin**[1,2,3], **Jurnie Rosius**[1], **Thomas R. Tedeschi**[4], **Oliver W. Gramlich**[3,4,5], **Randy H. Kardon**[3,4], **Isabella M. Grumbach**[1,2,3]

[1]Division of Cardiovascular Medicine, Abboud Cardiovascular Research Center, Department of Internal Medicine, Carver College of Medicine, University of Iowa, Iowa City, IA

[2]Department of Radiation Oncology, University of Iowa, Iowa City, IA

[3]Iowa City VA Center for the Prevention and Treatment of Visual Loss, Iowa City, IA

[4]Department of Ophthalmology and Visual Sciences, University of Iowa, Iowa City, IA

[5]Department of Neuroscience and Pharmacology, University of Iowa, Iowa City, IA

## Abstract

**Purpose:** To characterize the neuronal and vascular pathology *in vivo* and *in vitro* in a mouse model of radiation retinopathy.

**Methods:** C57Bl/6J mice underwent cranial irradiation with 12 Gy and *in vivo* imaging by optical coherence tomography and of relative blood flow velocity by laser speckle flowgraphy for up to 3 to 6 months after irradiation. Retinal architecture, vascular density and leakage and apoptosis were analyzed by histology and immunohistochemistry before irradiation or at 10, 30, 240, and 365 days after treatment.

**Results:** The vascular density decreased in the plexiform layers starting at 30 days after irradiation. No impairment in retinal flow velocity was seen. Subtle perivascular leakage was present at 10 days, in particular in the outer plexiform layer. This corresponded to increased width of this layer. However, no significant change in the retinal thickness was detected by OCT-B scans. At 365 days after irradiation, the nuclear density was significantly reduced compared to baseline. Apoptosis was detected at 30 days and less prominent at 365 days.

**Conclusions:** By histology, vascular leakage at 10 days was followed by increased neuronal apoptosis and loss of neuronal and vascular density. However, *in vivo* imaging approaches that are commonly used in human patients did not detect pathology in mice.

### Keywords

radiation retinopathy; mouse; apoptosis; capillaries

**Corresponding author:** Isabella Grumbach, MD, PhD, FAHA, Division of Cardiovascular Medicine, Department of Internal Medicine, Carver College of Medicine, University of Iowa, Iowa City, IA, 52242, isabella-grumbach@uiowa.edu.

## 1. INTRODUCTION

Brachytherapy using episcleral $^{125}$I seed-filled plaques is the standard treatment for uveal melanoma, the most common primary intraocular cancer in adults (Group, 2006). However, the multicenter Collaborative Ocular Melanoma Study (COMS) and other trials demonstrated that at least 50% of patients treated with brachytherapy experience significant vision loss within 3–5 yr after therapy (Group, 2006),(Melia et al., 2001, Aziz et al., 2016, Melia et al., 2006, Shields et al., 2000). The COMS reported extensive pathology after 2 yr or more in the normal retinal tissue that surrounded the melanoma (Boldt et al., 2009). An accepted, but incompletely tested concept is that radiation retinopathy is driven by microangiopathy that is initiated by the immediate damage to the microvascular endothelium during radiation.

Despite observations in humans consistent with early microvascular leakage and loss of microvascular and neuronal density years after therapy, few animal studies have been conducted to establish the mechanisms of radiation retinopathy. Several animal studies have reported on pathology after radiation of the eye, including photoreceptor damage and capillary loss (Archer et al., 1991, Amoaku et al., 1989, Irvine and Wood, 1987). These studies were conducted in a variety of species such as monkey, pig, cat and rat (Singh et al., 2012, Gragoudas et al., 1979). However, they have important limitations. In most studies, the main readout was descriptive histology rather than quantification (Irvine and Wood, 1987, Archer et al., 1991). In others, the main readouts were only obtained once at the end of the study. Only a few studies used mice based on the notion that ocular complications of radiation therapy are subtle in mice. Of these studies, most examined tumor control as opposed to microvascular and neuronal injury of the normal retinal tissue (Sobrin et al., 2004, Murray et al., 1996).

Establishing the stages of radiation retinopathy in mice is a prerequisite for preclinical testing of potential treatments. The lack of these data in mice is a major obstacle to capitalizing on the many available genetic models that could inform on molecular pathways and cell type specific contributions. Of note, no specific preventive treatment for radiation retinopathy is currently available, in part because the molecular and cellular drivers of radiation retinopathy are not well understood. Anti-VEGF therapy in humans has gained traction in the field supported by reports of decreased vision loss and macular edema after scheduled injections (Shah et al., 2014, Shields et al., 2020). However, microvascular density or retinal thickness were not affected (Eandi et al., 2021).

To fill some of these gaps, we sought to establish vascular and neuronal pathology in mice after cranial irradiation, specifically, evidence for early vascular leakage and late rarefication as well as neuronal cell death by apoptosis. We also tested whether OCT and laser speckle flowgraphy, *in vivo* imaging techniques that have recently been used in humans to investigate radiation retinopathy, can be deployed to characterize radiation retinopathy in mice.

## 2. MATERIAL AND METHODS

### 2.1. Mice

All experimental procedures were approved by the Institutional Animal Care and Use Committees of both the University of Iowa and the Iowa City VA Health Care System and complied with the standards of the Institute of Laboratory Animal Resource, National Academy of Science. Experiments were performed on C57BL/6J mice (Jackson Laboratories, #000664) which were between 10–22 weeks of age at the time of treatment.

### 2.2. Radiation exposure

Mice were anesthetized by IP injection of 17.5 mg/mL ketamine/2.5 mg/mL xylazine solution (VetaKet/AnaSed, 0.1 mL/20 g body weight) before receiving a single 12 Gy dose of X-rays (IR) to the brain and eyes. This treatment was administered using an XStrahl Small Animal Radiation Research Platform (SARRP), which incorporates a 60 kVp beam of 0.2 mm Al quality for Cone Beam CT acquisition and a 220 kVp 0.63 mm Cu quality beam for treatment-type IR. We established that this dose induces functional impairment of photoreceptors 30 days after irradiation.

### 2.3. Embedding and sectioning

Mice were euthanized at set time points post-irradiation by carbon dioxide inhalation followed by cervical dislocation: 11 mice (6 male, 5 female) at 10 d, 12 mice (7 male, 5 female) at 30 d, 9 mice (5 male, 4 female) at 240 d, and 11 mice (8 male, 3 female) at 365 d post-IR. An additional 16 mice (12 male, 4 female) that were not irradiated were included as controls. Eyes were harvested and drop-fixed in 4% paraformaldehyde for at least 24 hours before processing. Eyes were processed by removing the cornea, lens, and iris. Eyes were then cryo-embedded in Tissue-Tek® O.C.T. Compound and flash frozen using the Stand-Alone Gentle Jane® snap-freezer. Sagittal cross-sections were obtained using a cryostat microtome at a thickness of 10 μm. Slides were stored at −80°C until use.

### 2.4. Histology

Slides were fixed in pre-cooled 10% Zinc Formalin Fixative for 10 minutes prior to conventional hematoxylin and eosin staining. Slides were mounted with Permount™ Mounting Medium (Fisher Chemical, SP15) and cured at room temperature for at least 24 hours before imaging.

### 2.5. Immunofluorescent imaging

Immunofluorescent staining was performed using the following procedure unless otherwise noted: tissue sections were fixed, cryo-embedded, and sectioned as described above. Tissue samples were air-dried for 15 minutes, then rehydrated and fixed in 4% PFA in PBS for 15 min. Samples were washed in ddH2O twice for 5 minutes each and once with PBS 1X for 5 minutes. Samples were permeabilized and blocked for 1 hour using a solution of 0.3% Triton-X 100 and 5% normal donkey serum in PBS 1X (Solution A). Samples were then incubated in Tomato Lectin (DyLight 488, Vector Labs, DL-1174-1) overnight at 4°C or donkey anti-mouse IgG (Alexa Fluor 647, Invitrogen, A-31571) diluted into Solution A for

1 hour at room temperature. Samples were then washed 3X for 5 minutes each with PBS 1X. Samples were then mounted using VectaShield Antifade Mounting Medium with DAPI (Vector, H-1200) and incubated for at least 1 hour at 4°C before being imaged.

For TUNEL staining, the following protocol was used: Tissue samples were air-dried for 15 minutes, then rehydrated and fixed in 4% PFA in PBS for 15 min. Samples were then washed in PBS 3 times for 5 minutes each. Samples were then stained using the Situ Cell Death TMR red Detection Kit (Roche, 12156792910) according to manufacturer's instructions beginning from the permeabilization step.

### 2.6. *In vivo* imaging by laser speckle flowgraphy (LSFG)

Serial imaging by laser speckle flowgraphy (LSFG) was performed as we recently reported (Tamplin et al., 2021a). Images were acquired in 10 mice (5 male, 5 female) before and 1, 4, 14, 30, 60, 90, 120, and 180 d post-IR. Before imaging, mice were anesthetized by IP injection of 17.5 mg/mL ketamine/2.5 mg/mL xylazine solution (VetaKet/AnaSed, 0.1 mL/20 g body weight) and placed on a heating pad controlled by a rectal temperature probe (PhysioSuite; Kent Scientific), to maintain core body temperature at 37 °C. The right eye was dilated with 0.5% topical tropicamide. Blood flow measurements were obtained using the laser speckle flowgraphy device LSFG-Micro (Softcare Co., Ltd.) and coupled with a diffuse light flicker stimulus to invoke hyperemic response per our previously-established protocol (Tamplin et al., 2022a). Briefly, after an initial 50 s baseline recording period, a white light emitting-diode (LED) array (KICK LED, Rift Labs; 5000 K, 1200 lx, 10 Hz) affixed above the mouse eye was activated for 20 s, followed by 30 s of post-flicker recording. Blood flow measurements were acquired continuously (30 fps), with temporal composites of the 3.2 × 2.5 $mm^2$ imaged area automatically generated every 10 s for analysis, resulting in 10 composite images and a continuum of 3000 data points.

### 2.7. Optical coherence tomography

OCT imaging was performed on 9 mice (5 male, 4 female) at 30 d post-IR, and 7 control mice (4 male, 3 female). Imaging was performed with a Spectralis SD-OCT (Heidelberg Engineering, Vista, CA) system coupled with a 25-diopter lens for mouse ocular imaging (Heidelberg Engineering). Mice were anesthetized by IP injection of 17.5 mg/mL ketamine/2.5 mg/mL xylazine solution (VetaKet/AnaSed, 0.1 mL/20 g body weight) and placed on a heating pad to maintain body temperature. Pupils were dilated using a 0.5% tropicamide solution. The cornea was moisturized with a saline solution, which was applied every 20 to 30 seconds. A single horizontal OCT scan centered on the optic disc was acquired in each eye.

### 2.8. Image analysis

For vessel density and leakage by lectin and IgG staining, regions of interest (ROIs) were drawn to cover the IPL+GCL and OPL segments. Within these sections, an area of image background was measured to calculate background noise. This value was subtracted from the image before measuring the mean grey value in each ROI.

For layer thickness by H&E staining, the distance between the inner borders of each layer was calculated. In ImageJ, five rulers were placed within each layer, then averaged together to calculate thickness of that layer. This analysis was performed in three consecutive sections from the same eye. The measurements from the three sections were averaged together to generate one value for each layer for that mouse.

For nuclear density by DAPI staining, images were binarized using the Phansalkar thresholding method (radius 15, "white objects on black background")(Phansalkar et al., 2011). In the resulting image, white pixels are attributed to nuclei. ROIs were drawn to cover the INL and ONL, and the number of pixels counted in each. The percentage of DAPI-positive pixels was calculated as the number of white pixels divided by the total number of pixels in the layer.

For apoptosis by TUNEL staining, ROIs were drawn to encompass the INL and ONL; within these margins, a smaller area of image background was used to calculate background noise for each layer. This value was subtracted from the image before measuring the mean grey value in each ROI.

For relative blood flow by LSFG, each data series was analyzed per our previously-reported protocol(Tamplin et al., 2022a). Briefly, an ROI covering the retinal vasculature, but not the optic nerve head, was placed on each composite scan of the 100 s acquisition period. The mean blur rate in the ROI was calculated at each frame of the time series. Baseline blood flow was calculated using the median of the 30 s of acquisition before flicker stimulation, while the percent flicker response was calculated as the percent change in blood flow from baseline levels to the maximum of the flicker response curve.

For layer thickness by SD-OCT, an individual unaware of the treatment performed the analysis. Scans were opened with the accompanying software (Eye Explorer v. 1.10.4.0, Heidelberg Engineering). A scan at 300 μm from either side of the optic disc center was used for analysis. At this point, rulers covering the inner (ILM to IPL), outer (OPL and below), and total retinal layers were drawn to calculate retinal thickness. The average of the two measurements was used to report retinal thickness of each layer.

### 2.9. Statistical analysis

Statistical analyses were performed using GraphPad Prism (v. 9.0.0, GraphPad Software). Data are expressed as mean ± SEM. Normal data distribution was assessed by D'Agostino-Pearson omnibus normality test. When normal distribution was present, data were analyzed by a two-tailed Student t-test or by ANOVA followed by appropriate correction. Otherwise, the Mann-Whitney or the Kruskal-Wallis test was used. A probability value $< 0.05$ was considered significant.

## 3. RESULTS

### 3.1. Loss of inner and outer plexiform vasculature occurs after irradiation

First, we assessed for microvascular rarefication and quantified the vascular density, particularly that of the inner and outer retina plexiform layers, at different timepoints after

irradiation. We anticipated a decrease in the vascular density as a result of the radiation treatment. Thus, we labeled the microvascular beds with Lectin TL. As expected, we detected lectin labeling mostly in the outer aspects of the inner plexiform (IPL) and outer plexiform layers (OPL). Over the time course of 365 d, a statistically significant reduction in vascular density was seen at 240 d post-irradiation in the IPL and at 30 d post-irradiation in the OPL (Figure 1A–C). Vascular pathology was verified in lectin-labeled retinal flat mount at 30 days after irradiation (Supplemental Figure 1). Of note, we measured an increase in vascular density at 365 d relative to IPL and OPL thickness that was reduced at that time point. Moreover, we tested for vascular leakage by immunofluorescent imaging after anti-IgG staining (Figure 1D, E). Subtle perivascular IgG extravasation was seen at 10 d and 30 d post-irradiation in the OPL, indicative of leakage. This data suggest that vascular density decreases post-irradiation, and leakage is present at 10 d post-irradiation.

### 3.2. Thinning of retinal layers after irradiation

To further investigate the effects of vasculopathy on the retinal architecture, we quantified the retinal layer thickness. We expected the plexiform layers to increase in thickness at early timepoints due to edema and perivascular leakage similar to findings in humans (Tamplin et al., 2021b) and thin out at later timepoints in parallel to the loss of vasculature. For this purpose, we analyzed the retinal layers in five locations adjacent to the optic disc in three consecutive H&E-stained sections. All measurements were averaged, and data reported per mouse (Figure 2A).

While the marked increase in the layer thickness at 10 d in the plexiform layers was not statistically significant, by 240 and 365 d layer thickness had reduced significantly compared to 10 d post-RT (Figure 2B–C). In the nuclear layers, reduced layer thickness was noted by 240 d in the ONL and 365 d in the INL compared to the eyes of nonirradiated control mice (Figure 2D–E).

To further characterize pathology in the nuclear layers, we analyzed nuclear density by labeling of nuclei with DAPI (Figure 3A, B). As anticipated, we found a decrease in the number of pixels identified as nuclei at 365 d in parallel to layer thinning (Figure 3C, D). Similar observations were made when we calculated the percentage of nuclear pixels per area (Figure 3E, F). These data suggest a loss of anatomical organization with increased free space between nuclei.

We further hypothesized that neuronal apoptosis drives neuronal loss. Increased apoptosis was detected in both nuclear layers, beginning at 30 d post-irradiation (Figure 4A–C). Apoptosis was still elevated at the 240 d timepoint but returned to levels seen in nonirradiated control mice by 365 d.

### 3.3. *In Vivo* imaging of retinal layer structure

Imaging by optical coherence tomography has become an important clinical tool to track radiation retinopathy. Thus, we performed OCT-B imaging of the retina in a separate cohort of mice and analyzed the inner (IPL, INL and GCL) and the outer (OPL and ONL) retina in non-irradiated control mice and mice at 30 days post-irradiation. Here, we detected no significant changes in the inner and outer retina or total retinal thickness as a result of

irradiation (Figure 5A–D). Because of cataract formation in the irradiated eyes, no imaging at timepoints beyond 30 d could be performed.

We recently described laser speckle flowgraphy as a method to estimate blood flow and to test assess neurovascular coupling the mouse retina (Tamplin et al., 2021a). We deployed these methods to test for functional changes in the vasculature after irradiation. Of note, in C57BL/6J mice, only the flow in larger retinal arterioles can be measured. We did not detect any significant changes in blood flow or flicker response after radiation exposure (Figure 6A–D).

## 4. DISCUSSION

This study aimed to characterize injury by radiation in the mouse retina. In contrast to the notion that mice are “resistant” to radiation injury, we detected vascular and neuronal changes by histology that recapitulate features of radiation retinopathy in humans. There are three main findings in our study: 1. Radiation-induced vascular injury with discrete leakage at early timepoints and reduced vascular density over time. 2. Neuronal apoptosis was present at a timepoint when vascular leakage occurs. 3. Apoptosis in nuclear layers preceded loss of retinal layer thickness. These findings demonstrate that features of radiation retinopathy occur in mice. In future studies, genetically modified strains can be deployed to investigate the pathophysiology of radiation retinopathy, for example, the contribution of endothelial injury in models with endothelium-specific genetic modifications.

In humans, radiation retinopathy has been characterized as a vasculopathy with initial leakage and edema as well as late capillary drop-out, non-perfusion, and retinal vessel occlusion (Tamplin et al., 2021b, Boldt et al., 2009, Wen et al., 2009, Shields et al., 2016, Veverka et al., 2015). Studies in larger animals such as pigs, dogs and monkey recapitulated these findings (Irvine and Wood, 1987, Gragoudas et al., 1979, Ching et al., 1990, Barakat et al., 2011, Singh et al., 2012). In rats, vasculopathy occurs after two months with edema and later vascular occlusion. In contrast, a small number of studies of radiation retinopathy has been conducted in mice. Our findings indicate a decrease in vascularity over time. We detected a relative increase in vascular density at 365 d when IPL and OPL were thinned as a result of adaptive retinal remodeling after apoptotic cell death. At 10 d after IR, we also detected very subtle perivascular leakage, a feature that is well established in humans after radiation exposure of the eye during $^{125}$I-plaque brachytherapy.

Cell death by apoptosis was detected mostly in the nuclear layers at 10 d to 240 d after IR. Some very discrete TUNEL labeling was seen in the plexiform layers, potentially in endothelial cells. Over time, in particular at 365 d, the nuclear layer thickness along with the nuclear pixel counts decreased. The observation of significant thinning of the ONL after gradually increasing apoptosis of the same layer implies progressive neuronal loss after IR, beginning with the significant apoptosis observed at 30 d that progressed to a maximum at 240 d post-IR. By 365 d, apoptosis and loss of photoreceptors may have occurred to significantly thin the layer. Whether neuronal cell death is driven by inflammation, potentially initiated through blood retinal leakage or occurs as a result of ischemia after microvessel loss cannot be established at this point. However, these findings set the stage for

further studies with genetic models or potential drugs. These findings are similar to reports in the neonatal murine retina after whole body radiation with 2 Gy or in adult mice with 16 Gy (Borges et al., 2004). Here, we provide a detailed analysis of its time course.

*In vivo* imaging with OCT and OCT angiography has become an integral care for patients after radiation injury or $^{125}$I-plaque brachytherapy for uveal melanoma. In our hands, these imaging techniques did not prove effective for studying radiation retinopathy in this mouse model. We recently proposed laser speckle flowgraphy as a new approach to detect early impairment of flow after therapy (Tamplin et al., 2022b). However, we did not detect any overt changes in blood flow (Figure 6). In our studies in humans after $^{125}$I-plaque brachytherapy, blood flow in normal retinal tissue was mostly decreased in capillaries and choroidal vessels (Tamplin et al., 2022b). In C57Bl/6 mice, due to retinal pigmentation, the flow is recorded mostly in larger superficial arteries and arterioles but not in capillaries and choroidal blood vessels (Tamplin et al., 2021a, Tamplin et al., 2022a). Additional studies in mouse strains with decreased retinal pigmentation may be warranted to detect blood flow changes in mice *in vivo.* By OCT B-scans, retinal layer thickness at 30 d after radiation was not significantly altered (Figure 5), likely because the changes seen by histology are too subtle to detect by OCT-B in mice due to limitations of image resolution. Importantly, perhaps because the lens occupies a larger volume of the mouse eye compared to humans and other mammals (Ramos et al., 2019), significant radiation cataract formed 1–2 months post-IR; this prevented OCT imaging at time points past 30 d, and may limit the use of OCT imaging in mouse studies of radiation retinopathy.

Our findings reveal that radiation retinopathy can be detected in mice after exposure to a radiation dose that corresponds to approximately 40 Gy. Subtle early vascular leakage within the first 10 d after radiation is followed by apoptosis in the nuclear layers as well as loss of vascular density in the plexiform layers for up to 240 days after treatment. At 365 d post-radiation, retinal remodeling with loss of retinal thickness, particularly in the plexiform layers, has occurred. While this study establishes a time course and describes vascular and neuronal pathologies with findings similar to that in humans (Tamplin et al., 2021b, Veverka et al., 2015, Say et al., 2016), our findings do not establish causal relationships, for example whether decreased capillary density causes the loss of local neurons. Moreover, we did not study how neuroinflammation interacts with the time course of vascular and neuronal pathology in this model (Alt et al., 2014, Han et al., 2016). However, our findings provide a framework for further studies in which cell-type selective genetic models can be deployed, for example mice in which putative disease-modifying genes are deleted in microglia or in endothelial cells. These studies will be invaluable for the development of new therapies to prevent or treat radiation retinopathy.

## Supplementary Material

Refer to Web version on PubMed Central for supplementary material.

## ACKNOWLEDGEMENTS

The authors wish to thank Dr. Matthew Harper for his assistance with the OCT imaging and analysis as well as Dr. Christine Blaumueller, Scientific Editing and Research Communication Core, University of Iowa, for editorial assistance.

### FUNDING SOURCES

This study was supported by funding by the American Heart Association (18IPA34170003 to IMG; 20PRE35110054 to MRT), the National Institutes of Health (R01 EY031544 to IMG and RHK; T32 CA078586 to MRT), and the US Department of Veterans Affairs (I01BX000163 to IMG and I50RX003002 to RHK).

## REFERENCES

ALT C, RUNNELS JM, MORTENSEN LJ, ZAHER W & LIN CP 2014. In vivo imaging of microglia turnover in the mouse retina after ionizing radiation and dexamethasone treatment. Invest Ophthalmol Vis Sci, 55, 5314–9. [PubMed: 25082884]

AMOAKU WM, FREW L, MAHON GJ, GARDINER TA & ARCHER DB 1989. Early ultrastructural changes after low-dose X-irradiation in the retina of the rat. Eye (Lond), 3 (Pt 5), 638–46. [PubMed: 2630341]

ARCHER DB, AMOAKU WM & GARDINER TA 1991. Radiation retinopathy--clinical, histopathological, ultrastructural and experimental correlations. Eye (Lond), 5 (Pt 2), 239–51. [PubMed: 2070883]

AZIZ HA, SINGH N, BENA J, WILKINSON A & SINGH AD 2016. Vision Loss Following Episcleral Brachytherapy for Uveal Melanoma: Development of a Vision Prognostication Tool. JAMA Ophthalmol, 134, 615–20. [PubMed: 27101414]

BARAKAT MR, SHUSTERMAN M, MOSHFEGHI D, DANIS R, GERTNER M & SINGH RP 2011. Pilot study of the delivery of microcollimated pars plana external beam radiation in porcine eyes. Arch Ophthalmol, 129, 628–32. [PubMed: 21555617]

BOLDT HC, MELIA BM, LIU JC, REYNOLDS SM & GROUP COMS 2009. I-125 brachytherapy for choroidal melanoma photographic and angiographic abnormalities: the Collaborative Ocular Melanoma Study: COMS Report No. 30. Ophthalmology, 116, 106–115.e1. [PubMed: 19118701]

BORGES HL, CHAO C, XU Y, LINDEN R & WANG JY 2004. Radiation-induced apoptosis in developing mouse retina exhibits dose-dependent requirement for ATM phosphorylation of p53. Cell Death Differ, 11, 494–502. [PubMed: 14752509]

CHING SV, GILLETTE SM, POWERS BE, ROBERTS SM, GILLETTE EL & WITHROW SJ 1990. Radiation-induced ocular injury in the dog: a histological study. Int J Radiat Oncol Biol Phys, 19, 321–8. [PubMed: 2394611]

EANDI CM, POLITO MS, SCHALENBOURG A & ZOGRAFOS L 2021. Eighteen-Month Results of Intravitreal Anti-Vascular Endothelial Growth Factor on Vision and Microcirculation in Radiation Maculopathy. Retina, 41, 1883–1891. [PubMed: 33411473]

GRAGOUDAS ES, ZAKOV NZ, ALBERT DM & CONSTABLE IJ 1979. Long-term observations of proton-irradiated monkey eyes. Arch Ophthalmol, 97, 2184–91. [PubMed: 116637]

GROUP COMS 2006. The COMS randomized trial of iodine 125 brachytherapy for choroidal melanoma: V. Twelve-year mortality rates and prognostic factors: COMS report No. 28. Arch Ophthalmol, 124, 1684–93. [PubMed: 17159027]

HAN W, UMEKAWA T, ZHOU K, ZHANG XM, OHSHIMA M, DOMINGUEZ CA, HARRIS RA, ZHU C & BLOMGREN K 2016. Cranial irradiation induces transient microglia accumulation, followed by long-lasting inflammation and loss of microglia. Oncotarget, 7, 82305–82323. [PubMed: 27793054]

IRVINE AR & WOOD IS 1987. Radiation retinopathy as an experimental model for ischemic proliferative retinopathy and rubeosis iridis. Am J Ophthalmol, 103, 790–7. [PubMed: 2438938]

MELIA BM, ABRAMSON DH, ALBERT DM, BOLDT HC, EARLE JD, HANSON WF, MONTAGUE P, MOY CS, SCHACHAT AP, SIMPSON ER, STRAATSMA BR, VINE AK, WEINGEIST TA & GROUP COMS 2001. Collaborative ocular melanoma study (COMS)

randomized trial of I-125 brachytherapy for medium choroidal melanoma. I. Visual acuity after 3 years COMS report no. 16. Ophthalmology, 108, 348–66. [PubMed: 11158813]

MELIA M, MOY CS, REYNOLDS SM, HAYMAN JA, MURRAY TG, HOVLAND KR, EARLE JD, KURINIJ N, DONG LM, MISKALA PH, FOUNTAIN C, CELLA D, MANGIONE CM & GROUP COMS-QOLS 2006. Quality of life after iodine 125 brachytherapy vs enucleation for choroidal melanoma: 5-year results from the Collaborative Ocular Melanoma Study: COMS QOLS Report No. 3. Arch Ophthalmol, 124, 226–38. [PubMed: 16476893]

MURRAY TG, ROTH DB, O'BRIEN JM, FEUER W, CICCIARELLI N, MARKOE AM, HERNÁNDEZ E, SMITH BJ & WINDLE JJ 1996. Local carboplatin and radiation therapy in the treatment of murine transgenic retinoblastoma. Arch Ophthalmol, 114, 1385–9. [PubMed: 8906029]

PHANSALKAR N, MORE S, SABALE AM & JOSHI M 2011. Adaptive local thresholding for detection of nuclei in diversity stained cytology images. 2011 International Conference on Communications and Signal Processing, 218–220.

RAMOS MS, ECHEGARAY JJ, KUHN-ASIF S, WILKINSON A, YUAN A, SINGH AD & BROWNE AW 2019. Animal models of radiation retinopathy - From teletherapy to brachytherapy. Exp Eye Res, 181, 240–251. [PubMed: 30716328]

SAY EA, SAMARA WA, KHOO CT, MAGRATH GN, SHARMA P, FERENCZY S & SHIELDS CL 2016. PARAFOVEAL CAPILLARY DENSITY AFTER PLAQUE RADIOTHERAPY FOR CHOROIDAL MELANOMA: Analysis of Eyes Without Radiation Maculopathy. Retina, 36, 1670–8. [PubMed: 27232466]

SHAH SU, SHIELDS CL, BIANCIOTTO CG, ITURRALDE J, AL-DAHMASH SA, SAY EAT, BADAL J, MASHAYEKHI A & SHIELDS JA 2014. Intravitreal bevacizumab at 4-month intervals for prevention of macular edema after plaque radiotherapy of uveal melanoma. Ophthalmology, 121, 269–275. [PubMed: 24139123]

SHIELDS CL, DALVIN LA, CHANG M, MAZLOUMI M, FORTIN P, MCGARREY M, MARTIN A, YAGHY A, YANG X, VICHITVEJPAISAL P, MASHAYEKHI A & SHIELDS JA 2020. Visual Outcome at 4 Years Following Plaque Radiotherapy and Prophylactic Intravitreal Bevacizumab (Every 4 Months for 2 Years) for Uveal Melanoma: Comparison With Nonrandomized Historical Control Individuals. JAMA Ophthalmol, 138, 136–146. [PubMed: 31830238]

SHIELDS CL, SAY EA, SAMARA WA, KHOO CT, MASHAYEKHI A & SHIELDS JA 2016. OPTICAL COHERENCE TOMOGRAPHY ANGIOGRAPHY OF THE MACULA AFTER PLAQUE RADIOTHERAPY OF CHOROIDAL MELANOMA: Comparison of Irradiated Versus Nonirradiated Eyes in 65 Patients. Retina, 36, 1493–505. [PubMed: 26960015]

SHIELDS CL, SHIELDS JA, CATER J, GUNDUZ K, MIYAMOTO C, MICAILY B & BRADY LW 2000. Plaque radiotherapy for uveal melanoma: long-term visual outcome in 1106 consecutive patients. Arch Ophthalmol, 118, 1219–28. [PubMed: 10980767]

SINGH RP, SHUSTERMAN EM, MOSHFEGHI D, DANIS R & GERTNER M 2012. Pilot study of the delivery of microcollimated pars plana external beam radiation in porcine eyes: 270-day analysis. J Ophthalmol, 2012, 615214. [PubMed: 22848793]

SOBRIN L, HAYDEN BC, MURRAY TG, CICCIARELLI N, SCOTT IU, HERNANDEZ E, WU X, MARKOE AM, FEUER W, FULTON L & O'BRIEN JM 2004. External beam radiation "salvage" therapy in transgenic murine retinoblastoma. Arch Ophthalmol, 122, 251–7. [PubMed: 14769602]

TAMPLIN MR, BROADHURST KA, VITALE AH, HASHIMOTO R, KARDON RH & GRUMBACH IM 2021a. Longitudinal Testing of Retinal Blood Flow in a Mouse Model of Hypertension by Laser Speckle Flowgraphy. Transl Vis Sci Technol, 10, 16.

TAMPLIN MR, BROADHURST KA, VITALE AH, HASHIMOTO R, KARDON RH & GRUMBACH IM 2022a. Measuring hyperemic response to light flicker stimulus using continuous laser speckle flowgraphy in mice. Exp Eye Res, 216, 108952. [PubMed: 35051429]

TAMPLIN MR, DENG W, GARVIN MK, BINKLEY EM, HYER DE, BUATTI JM, LEDOLTER J, BOLDT HC, KARDON RH & GRUMBACH IM 2021b. Temporal Relationship Between Visual Field, Retinal and Microvascular Pathology Following 125I-Plaque Brachytherapy for Uveal Melanoma. Invest Ophthalmol Vis Sci, 62, 3.

TAMPLIN MR, WANG JK, VITALE AH, HASHIMOTO R, GARVIN MK, BINKLEY EM, HYER DE, BUATTI JM, BOLDT HC, KARDON RH & GRUMBACH IM 2022b. Reduced blood flow by laser speckle flowgraphy after (125)I-plaque brachytherapy for uveal melanoma. BMC Ophthalmol, 22, 285. [PubMed: 35765019]

VEVERKA KK, ABOUCHEHADE JE, IEZZI R & PULIDO JS 2015. NONINVASIVE GRADING OF RADIATION RETINOPATHY: The Use of Optical Coherence Tomography Angiography. Retina, 35, 2400–10. [PubMed: 26502009]

WEN JC, OLIVER SC & MCCANNEL TA 2009. Ocular complications following I-125 brachytherapy for choroidal melanoma. Eye (Lond), 23, 1254–68. [PubMed: 19265865]

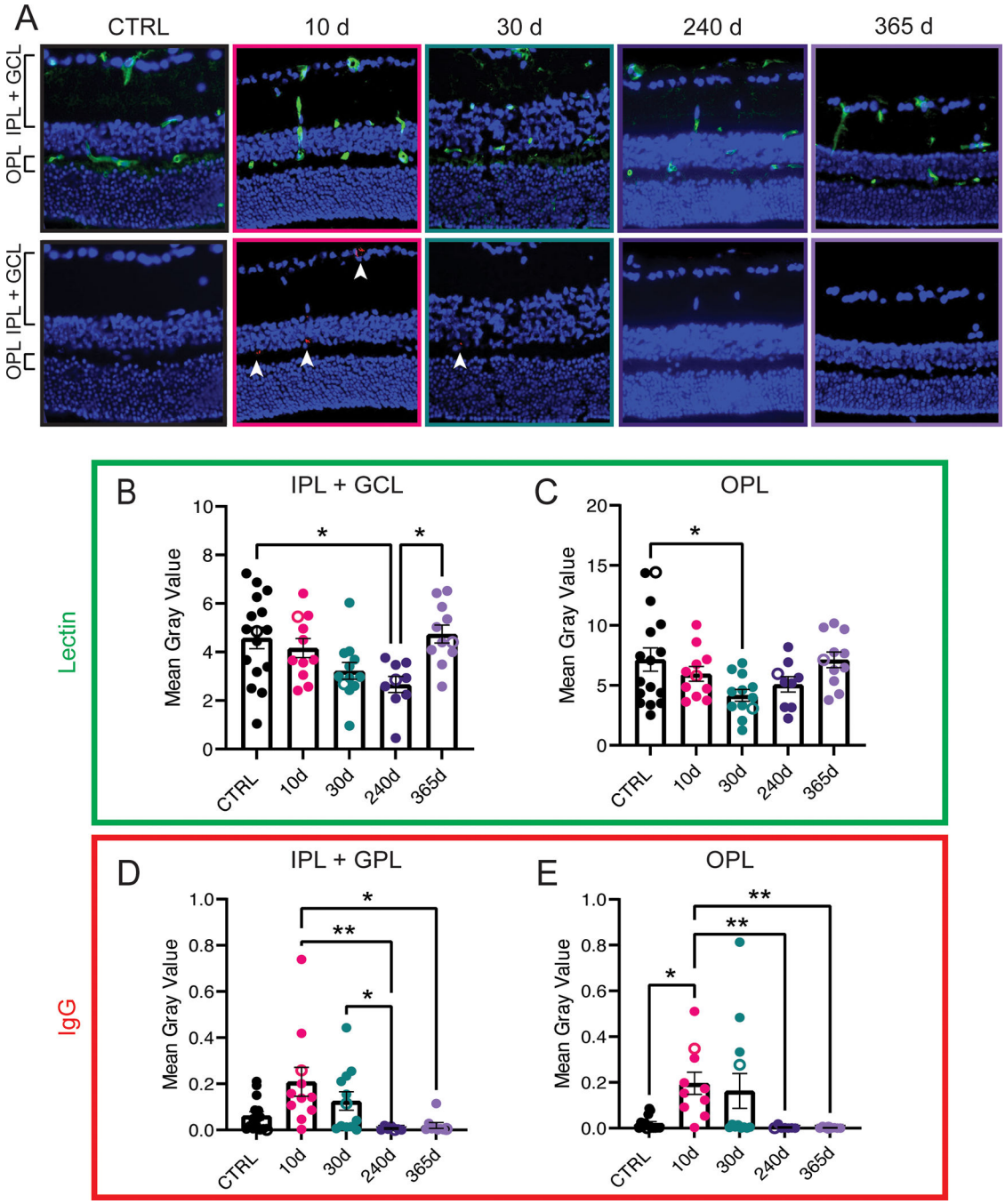


**Figure 1: Perivascular leakage and decreased vessel density after irradiation.**

(**A**) Ten-μm transverse sections of the mouse retina adjacent to the optic nerve head were stained with lectin TL (green, top) or IgG (red, bottom) and DAPI (blue). Magnification 20X, scale bar 100 μm. All images were captured in within 200 μm from the optic nerve head with the same settings and post-processing. (**B, C**) Mean gray value of lectin labeling in the inner (**B**) and outer plexiform layer (**C**) as a measure of staining intensity per area. (**D, E**) Mean gray value of IgG immunofluorescence in the inner (**D**) and outer plexiform layer (**E**) as a measure of staining intensity per area. Error bar indicates mean +/− SEM. *

$p < 0.05$, ** $p < 0.01$ by ordinary one-way ANOVA with Tukey's multiple comparisons test (**B, C**), or Kruskal-Wallis test with Dunn's multiple comparisons test (**D, E**). Data points represented by open circles in (**B-E**) correspond to images in (**A**).

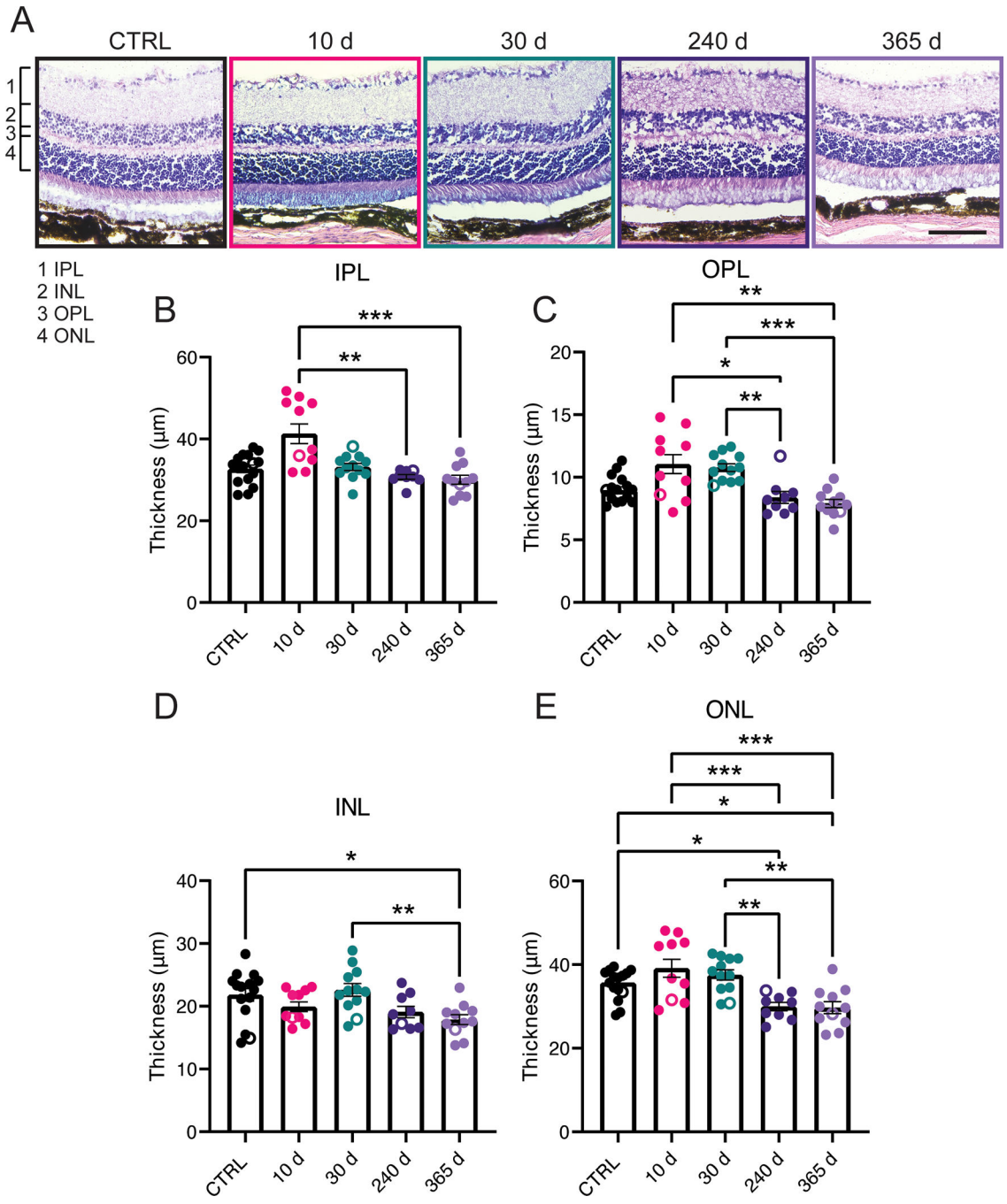


**Figure 2: Variations in layer thickness by hematoxylin and eosin staining.**

(**A)** H&E staining of 10-µm transverse sections of the mouse retina adjacent to the optic nerve head. Five measurements of each layer were averaged per section. (**B-E**) Quantification of layer thickness of the inner (IPL, **B**) and outer plexiform layer (OPL, **C**) and inner (INL, **D**) and outer nuclear layer (ONL, **E**). Error bar indicates mean +/− SEM. Magnification 20X, scale bar 100 µm. * $p < 0.05$, ** $p < 0.01$ by ordinary one-way ANOVA with Holm-Šídák's multiple comparisons test (**B, D**), Kruskal-Wallis with Dunn's multiple

comparisons test (**C**), or one-way ANOVA with Tukey's multiple comparisons test (**E**). Data points represented by open circles in (**B**-**E**) correspond to images in (**A**).

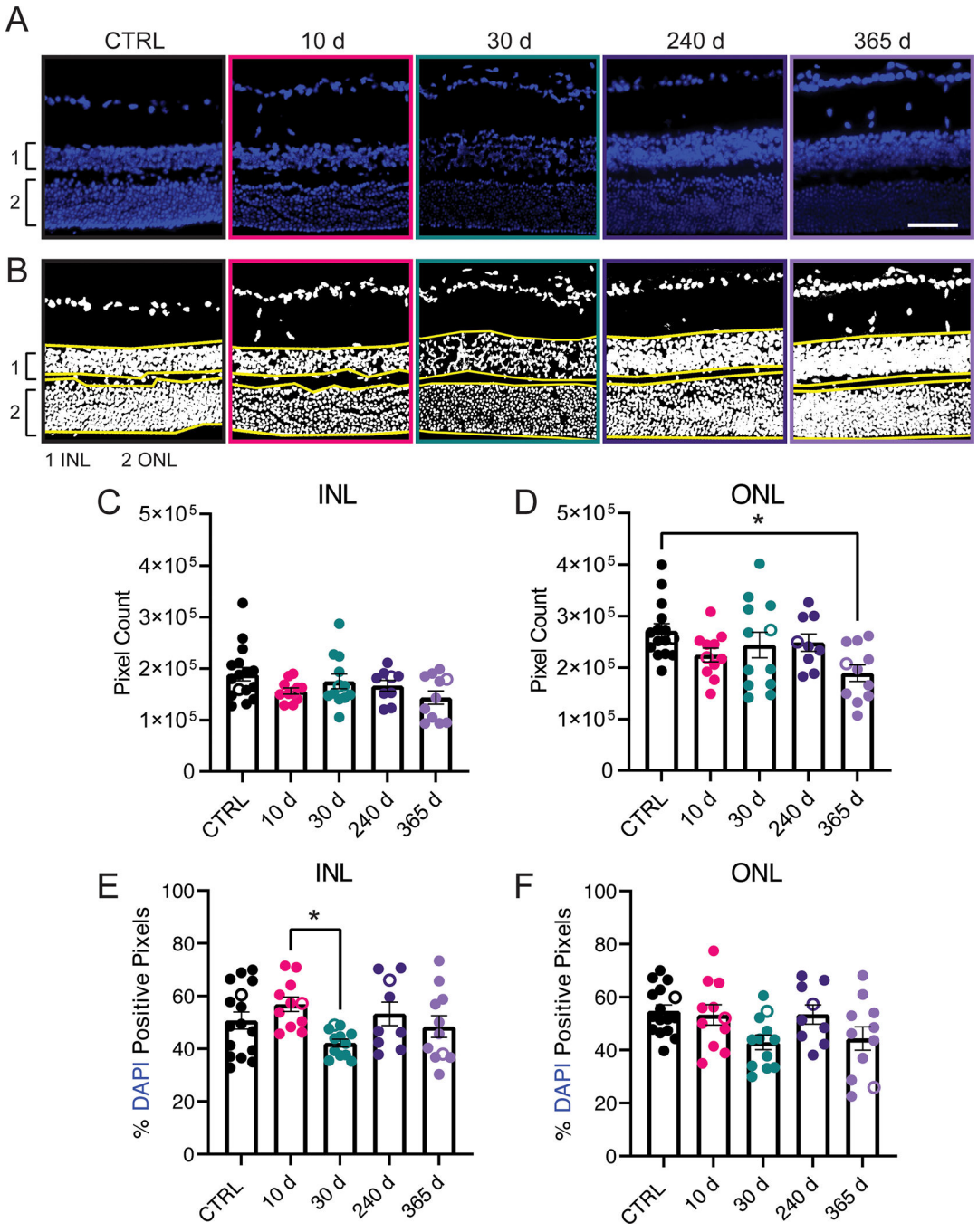


**Figure 3: Decreased outer nuclear density by 365 d post-irradiation.**

(**A**) Nuclear labeling by DAPI staining (blue) in the mouse retina at time points after irradiation as indicated. (**B**) Images were processed for cell counting using Phansalkar thresholding methods. (**C, D**) Quantification of layer thickness as a measure of pixel count per segment area for the inner (**B**) and outer (**C**) nuclear layers. (**E, F**) Quantification of DAPI signal as a measure of cell body density in the inner (**E**) and outer (**F**) nuclear layers. Magnification 20X, scale bar 100 μm. Error bar indicates mean +/− SEM. ** $p < 0.01$ by Kruskal-Wallis with Dunn's multiple comparisons test (**B**), or ordinary one-way ANOVA

with Tukey's multiple comparisons test (**C**). Data points represented by open circles in (**C-F**) correspond to images in (**A-B**).

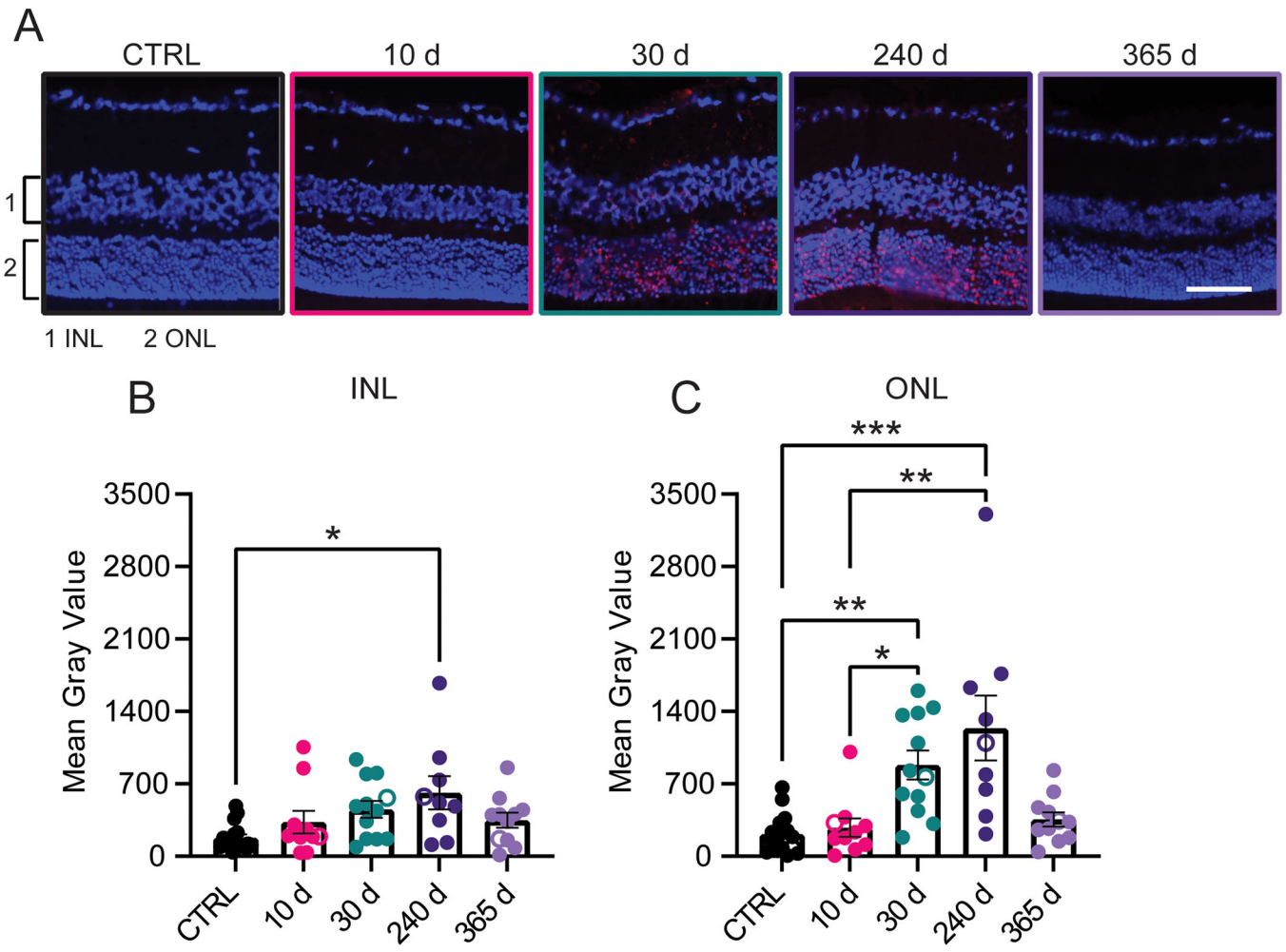


**Figure 4: Apoptosis after irradiation.**

(**A**) Representative images of TUNEL staining (red) and nuclear labeling (blue) in the mouse retina at time points after irradiation as indicated. Images and processing performed with identical settings for all time points. Magnification 20X, scale bar 100 μm. (**B, C**) Quantification of TUNEL-positive pixels in the inner (INL, **B**) and outer nuclear layer (ONL, **C**). Error bar indicates mean +/− SEM. * $p < 0.05$, ** $p < 0.01$, *** $p < 0.001$ by Kruskal-Wallis with Dunn's multiple comparisons test **(B, C**). Data points represented by open circles in (**B, C**) correspond to images in (**A**).

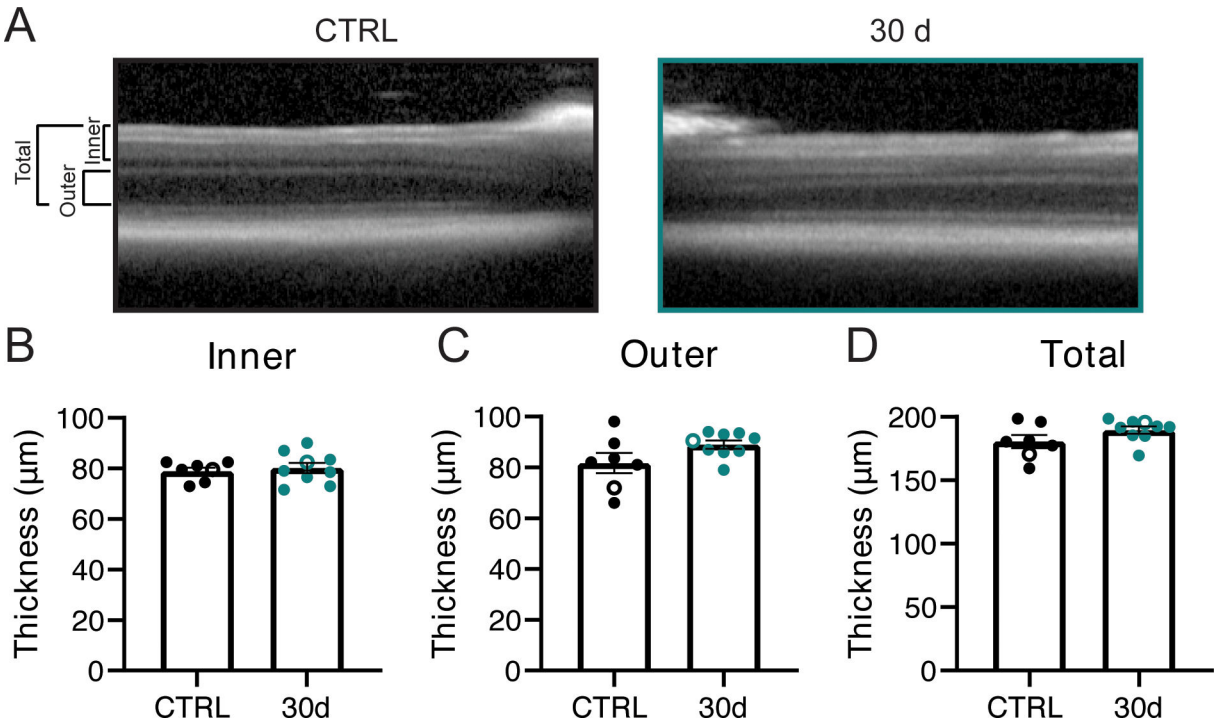


**Figure 5: *In vivo* assessment of retinal thickness before and 30 d after irradiation by OCT.**

(**A**) Representative OCT scans in the mouse retina before (left, black) and 30 d after irradiation (right, teal), cropped at the disc center to highlight retinal layer structure. Thickness was measured manually in the inner (**B**), outer (**C**), and total (**D**) retinal sections grouped as indicated in (**A**). Error bars indicate mean +/− SEM. Comparison nonsignificant by two-tailed unpaired t-test (**B-D**). Data points represented by open circles in (**B-D**) correspond to images in (**A**).

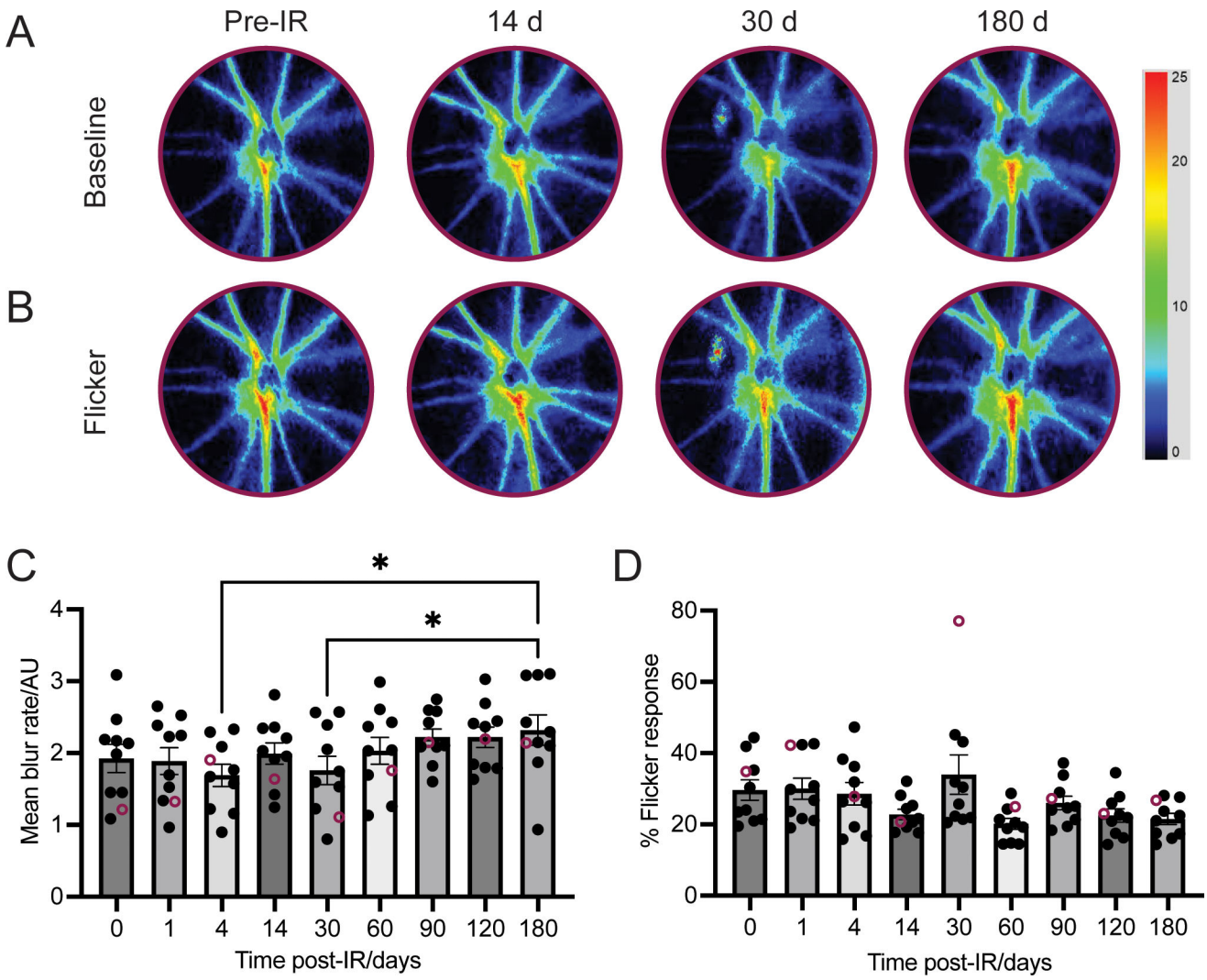


**Figure 6: Inner retinal blood flow does not change significantly by 180 d after irradiation.**

(**A, B**) Representative images taken during a baseline recording (**A**) and flicker stimulus (**B**) before irradiation and at 14, 30, and 180 d post-irradiation in a single mouse. Area between the two dashed lines was used to analyze inner retinal flow. (**C**) Quantification of retinal blood flow and (**D**) percent change in flow at peak response to flicker stimulus in 5 male and 5 female C57BL/6J mice before irradiation and at 8 sessions over a 180 d-period. Error bars indicate mean +/− SEM. * $p < 0.05$ by repeated measures one-way ANOVA with Holm-Šídák's multiple comparisons test. Data points represented by open circles in (**C-D**) correspond to images in (**A-B**).